



Additive Manufacturing and Characterization of Porous Ceramic Electrospray Emitters

Suhail Chamieh*, Elaine Petro[†] and Sadaf Sobhani[‡]
Cornell University, Ithaca, NY, 14850

This work presents a new approach for fabricating porous ceramic emitters using microscale 3D printing for electrospray thrusters and other applications. A method for tuning the ceramic's permeability through sintering is also presented. Direct current measurements in response to an applied voltage was used to characterize the emission of individual emitters with EMI-BF4. Radiography experiments were performed at a synchrotron facility to image capillary flow inside porous emitters during initial wetting.

I. Nomenclature

κ	=	permeability
ϕ	=	porosity
r_p	=	pore radius
r_g	=	grain radius
x	=	capillary rise
γ	=	surface tension
θ	=	solid-liquid contact angle
η	=	dynamic viscosity
h	=	height
α	=	half-angle
R_c	=	tip radius of curvature
Z	=	hydraulic impedance

II. Introduction

A porous emitter is a scaffold that guides a conductive liquid towards the apex of a sharp cone for extraction by an applied electric field. The emitted plume of ions can be used in several applications including in-space propulsion and attitude control[1], focused ion beam etching and deposition[2], and soft ionization mass spectrometry for identifying complex organic molecules[3].

To date, many manufacturing techniques have been employed to create porous electrospray emitters that can support stable ion emission from conductive liquids. These include electrochemical etching of porous tungsten [4], mechanical polishing of carbon xerogel [5] and laser ablation of porous silica [6]. All these processes are inherently subtractive manufacturing techniques which require separate processes for the emitter substrate formation and shaping. Prior to this point, additive manufacturing had not offered the print resolution to create parts with the micron-scale features required for electrospray propulsion.

This work leverages two-photon polymerization (TPP) to additively manufacture electrospray emitters. TPP uses a femtosecond pulsed IR laser to polymerize sub-micron focal volumes inside a liquid resin [7]. Polymerization is activated when two IR photons are near simultaneously absorbed by the photo-initiator and occurs only near the focal point where the laser intensity is highest. The induced nm-scale voxel allows the laser to print parts with nano and micron-scale features [8]. A TPP-based polymer printer is used in this work to create conical molds and produce emitters with external geometries suitable for electrospray emission.

*Graduate Student, Mechanical and Aerospace Engineering, AIAA Student Member

[†]Assistant Professor, Mechanical and Aerospace Engineering, AIAA Member.

[‡]Assistant Professor, Mechanical and Aerospace Engineering, AIAA Member.

III. Fabrication

The general fabrication steps are shown in Fig. 1. Emitters are shaped by casting a ceramic slurry inside a 3D printed mold. This mold, which takes the complimentary shape of the emitter, is printed on a Nanoscribe GT2 from IP-S resin over an acrylic substrate using the 25x objective lens. The substrate includes a small through hole in the center to facilitate development and a larger hole that acts as a mold for the emitter base. After printing, the mold and substrate are submerged in PGMEA for 3 hours followed by IPA for 1 hour, to wash away uncured resin. After drying and post-curing, the mold is filled with a commercial alumina slurry (AdmaPrint A130) and placed in a desiccator to evacuate any trapped air. The substrate is then flooded with UV on both sides to harden the slurry inside the mold. At this point the substrate goes through three stages of heat treatment. The first step burns off the bulk of the mold and substrate. It consists of a 600°C/hr ramp to 600°C and is held there for 2 hours. The second step vaporizes the remaining binder in the ceramic following a standard alumina debinding program. The third step partially sinters the ceramic following a standard sintering program except the maximum sintering temperature is reduced to partially sinter and preserve the porous matrix leftover from debinding. The second and third program follow Admatec's general guidelines.

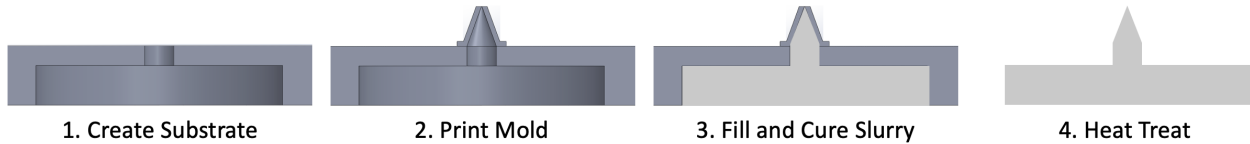


Fig. 1 Fabrication process steps.

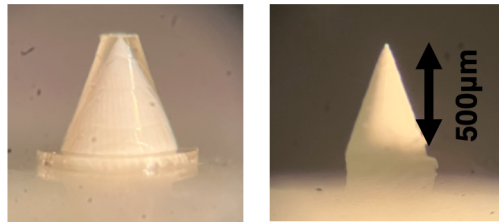


Fig. 2 Mold filled with slurry (step 3) and the resulting emitter (step 4).

Through 3D printing, the emitter's external geometry can be chosen without modifying the fabrication process. Furthermore, by tuning the sintering curve, the emitter's permeability can be tuned as well, as demonstrated in the next section. Emission characteristics of a porous emitter depend on its hydraulic impedance, which is a function of its external geometry and permeability [5] and is given by

$$Z = \frac{\eta}{2\pi\kappa} \frac{1}{1 - \cos\alpha} \left(\frac{\tan\alpha}{R_c} - \frac{\cos\alpha}{h} \right) \quad (1)$$

where h is the height of the emitter, α is the half angle, R_c is the tip radius of curvature, κ is the permeability of the substrate and η is the viscosity of the ionic liquid (27.5 mPa s for EMI-BF4). In the fabrication of our test emitters, we targeted a hydraulic impedance exceeding 1.5×10^{17} kg s⁻¹ m⁻⁴ that would be consistent with pure ion emission with EMI-BF4 [9]. For a mold designed to produce emitters with $h = 500 \mu\text{m}$, $\alpha = 20^\circ$ and $R_c = 20 \mu\text{m}$, the permeability should remain below $8 \times 10^{-15} \text{ m}^2$.

The external geometry and permeability can be verified through SEM imaging, an example of which is shown in Fig. 3. The fabrication approach developed in this work aims to control both variables to achieve the desired emission behavior.

IV. Characterization

A. SEM Imaging

The ceramic's final microstructure is largely determined during sintering. At elevated temperatures, atoms that make up the ceramic crystals in the powder particles diffuse across crystal boundaries and fuse the particles together

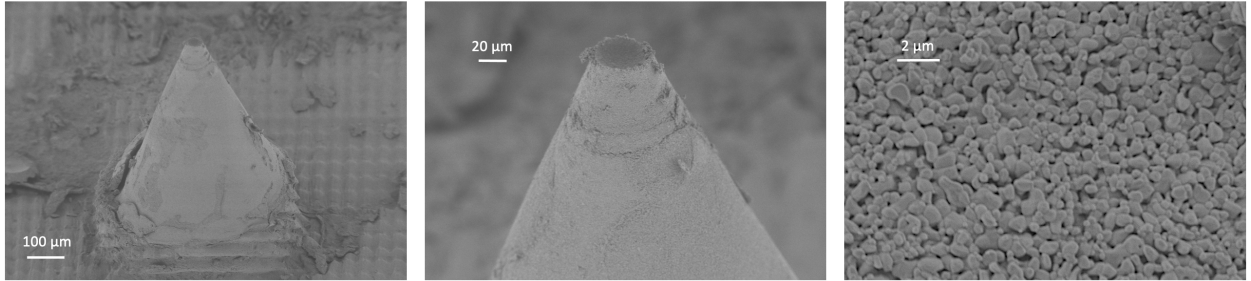


Fig. 3 SEM images of a sintered alumina emitter.

[10]. The extent of which is determined by the maximum sintering temperature and dwell time. In this experiment, only the maximum sintering temperature was varied. The lower the temperature, the smaller the grains and the greater the void space. The higher the temperature, the denser the ceramic, the lower the permeability. An example of the range of permeabilities and pore sizing achieved is shown in Fig. 4.

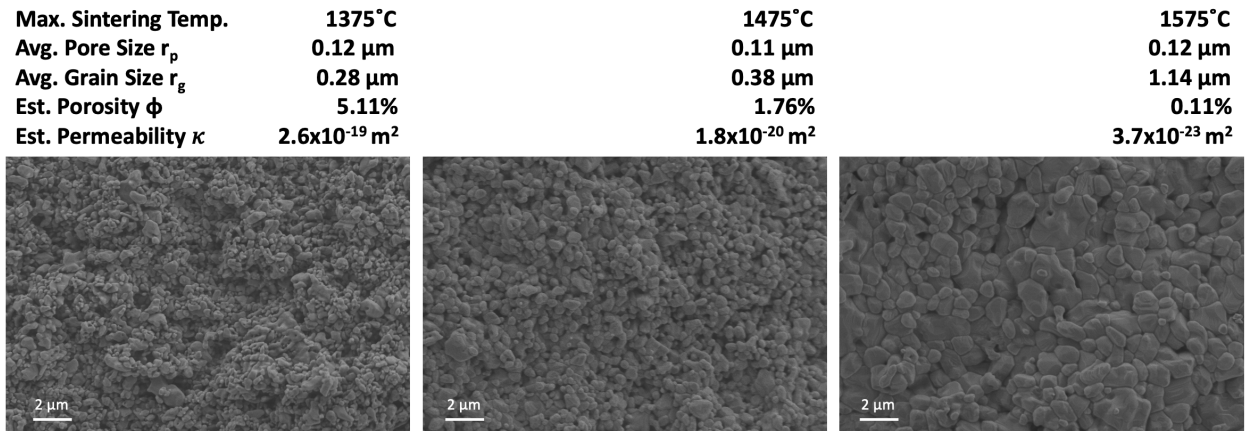


Fig. 4 SEM images of alumina sintered at various temperatures, demonstrating modulation of permeability.

Based on SEM inspection of broken emitters, this work assumes that the external surface features observed through SEM are representative of the emitter's internal structure. Images of the microstructure were analyzed using ImageJ. The average pore radius was obtained by thresholding the image to isolate the darker pores from the brighter grains. The individual pore areas were then measured, averaged and the radius was found by assuming the area to be circular. The porosity was obtained by taking the ratio of the pore volume to the total volume of pores and grains. In this estimate, the pores and grains were considered spherical and assigned radii based on their areas. The grains areas were measured after segmenting the image using a watershed algorithm. Finally, the permeability was computed using the Kozeny-Carman equation [11] with the grains assumed to be spherical, and is given by

$$\kappa = \frac{\phi^3 (2r_g)^2}{180(1 - \phi)^2} \quad (2)$$

where ϕ is the volumetric porosity of the substrate and r_g is the average grain radius.

B. X-Ray Imaging

Porous emitters passively absorb propellant from a downstream reservoir and wick it to the emission site by capillary action. X-ray imaging of the wetting process was performed at Argonne National Laboratory using the Advanced Photon Source 2-BM. This approach allows us to visualize the liquid traveling to the tip of the emitter during the initial wetting process. During the experiment, a high flux collimated beam of 30 keV x-rays were directed to the emitter as it passively absorbed the solution, and were recorded at their exit by a detector. The emitter was wetted from below the porous

cylindrical base it rests on with a saturated solution of potassium iodide (for contrast) using a micropump that filled a reservoir underneath the base. The micro-pump was remotely turned off after filling the reservoir to make sure the flow upstream was driven by capillary force alone. A time-series exposure of the wetting process observed through x-ray imaging is shown in Fig. 5. To highlight the flow, the dry emitter background was subtracted during post-processing.

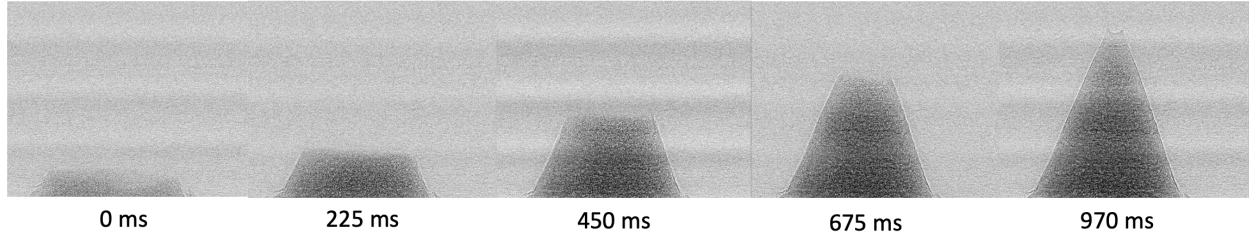


Fig. 5 X-ray images of the traveling liquid front.

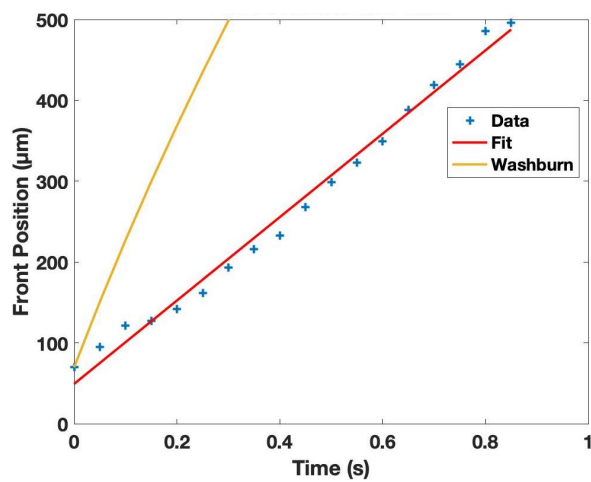


Fig. 6 Plot of the liquid front position over time.

The liquid rise in the emitter was filmed at 300 frames/s with a pixel resolution of $0.46 \mu\text{m}$. To produce the plot shown in Fig. 6, the height of the front was manually measured in ImageJ every 15 frames. The observed flow velocity, close to $500 \mu\text{m/s}$, was determined by applying a linear fit to the experimental data.

The Bosanquet equation can be used, to some extent, to describe the capillary rise in porous materials [12]. If we assume the flow is laminar ($\text{Re} \approx 10^{-4} \ll 1$) such that the viscous forces dominate inertial effects in the observed time frame (when the front reaches the base of the emitter) and ignore gravitational forces, the equation leads to the Washburn solution given by

$$x(t) = \sqrt{\frac{\gamma r_p \cos \theta}{2\eta}} t \quad (3)$$

where x represents the capillary rise as a function of time, γ the surface tension of the contrast solution ($\approx 10^{-1} \text{ N/m}$), r_p the pore radius ($\approx 0.12 \mu\text{m}$), θ the solid-liquid contact angle ($\approx 45^\circ$), and η the dynamic viscosity ($\approx 10^{-3} \text{ Pa/s}$). The Washburn solution is plotted in Fig. 6 beginning when the flow reaches the base of the emitter and defined at $t = 0$ s. In the observed time frame, the predicted capillary rise approximately models the observed linear relationship. However, the predicted Washburn velocity is higher, close to $1500 \mu\text{m/s}$. Because the Bosanquet equation is derived for capillary flow in vertical cylindrical channels, it fails to take into account the drag associated with the porous medium's tortuosity which would result in a lower flow velocity, bringing it closer to the measured value.

This experiment and brief analysis serves as a proof of concept for this new diagnostic capability which can potentially be employed to characterize previously inaccessible aspects of in-operando electrospray operation. For single emitters, beyond measuring the flow speed, x-ray imaging could provide more accurate information on the emitter's

permeability than through static SEM inspection alone. For arrays, tracking the wetting paths using x-ray computed tomography could help diagnose propellant transport problems that lead to partial wetting and guide the design of better wetting frameworks between the reservoir and array.

V. Performance

For ion plume characterization, emitters are mounted to conductive SEM stubs via carbon tape, wetted with an ionic liquid (EMI-BF4) and fitted onto a three-axis manual stage shown in Fig. 7. The stage allows the tip to be precisely positioned with respect to the extractor aperture before firing.

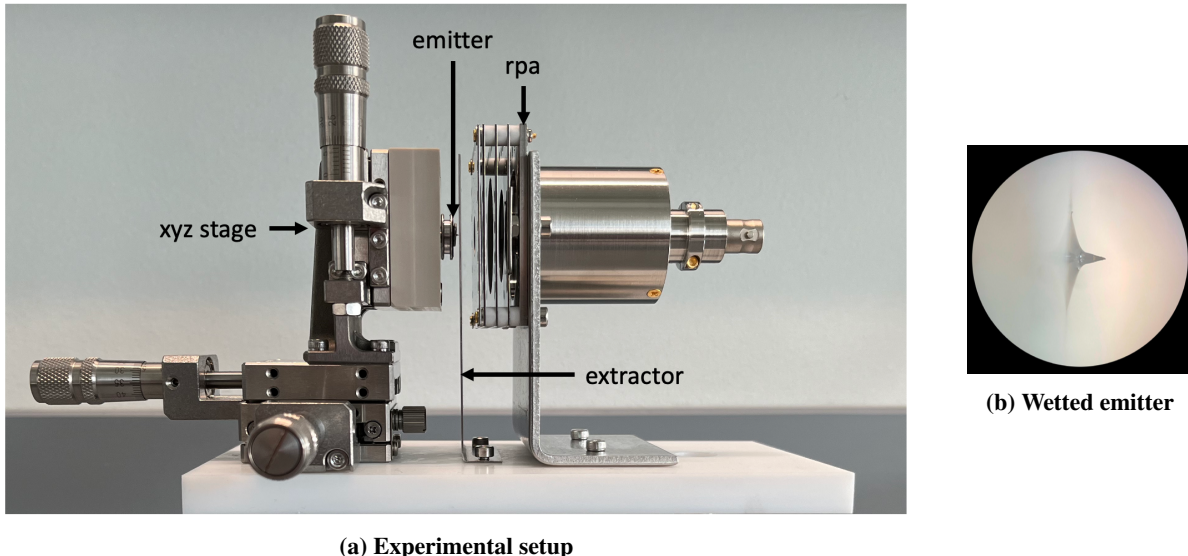


Fig. 7 Experimental setup configured for retarding potential analysis and current versus voltage characterization.

Figure 8 shows the current emitted as a function of applied voltage for a single emitter with a tip radius of curvature of $20 \mu\text{m}$ and a hydraulic impedance close to $10^{22} \text{ kg s}^{-1} \text{ m}^{-4}$. This emitter tip was continuously fired over the course of 70 minutes. The current was collected and subsequently averaged after applying a triangular voltage scan between $\pm 3 \text{ kV}$ at 10 V increments. The lingering time at each voltage varied between 1 and 5 seconds and was determined by the settling delay of the Keithley 2657A source meter used to supply the voltage and measure the emitted current from the source.

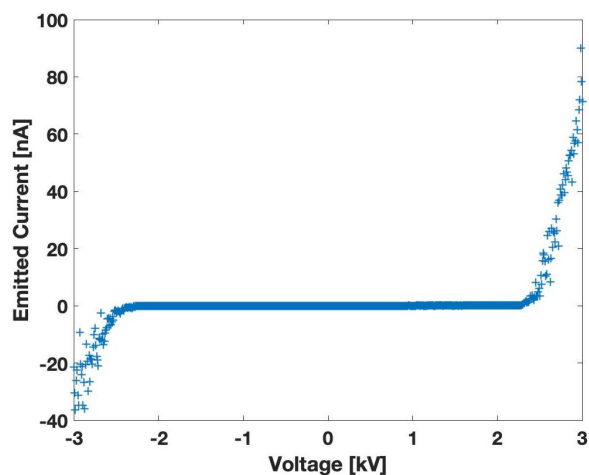


Fig. 8 Emitted current as a function of applied voltage.

Initial characterization of porous emitters indicates that currents on the order of 50 nA are emitted at typical operating voltages of 2 to 3 kV. A full characterization of the ceramic emitter will be performed in a future study.

VI. Conclusion

The fabrication process outlined in this work can create porous ceramic electrospray emitters that can support stable ion emission. To date the process has been developed for single emitters but can be readily extendable to emitter arrays. This work represents the first publication of the manufacturing process and characterization of electrospray emitters fabricated in this manner. Another unique aspect of this work is the use of x-ray imaging to track wetting and fluid flow through the porous substrate.

VII. Future Work

Future work will include time-of-flight mass spectrometry, retarding potential analysis and beam divergence measurements to fully characterize the plume and the emitter's performance. More sintering tests will be conducted over a larger set of maximum sintering temperatures to quantify the relationship between the sintering variable, pore characteristics and ion plume quality. The end goal is to develop a methodology that would enable direct control of the emitter hydraulic impedance and thereby the emission mode. Additionally, future efforts will extend the fabrication technique to arrays, and determine the bounds of scalability of the print technique. Finally, we seek to develop the use of x-ray imaging as a new diagnostic tool for emitter and array characterization.

Acknowledgments

This research used resources of the Advanced Photon Source, a U.S. Department of Energy (DOE) Office of Science user facility operated for the DOE Office of Science by Argonne National Laboratory under Contract No. DE-AC02-06CH11357. The authors thank Viktor Nikitin from the Advanced Photon Source 2-BM for his help with x-ray imaging acquisition and data processing. The authors also thank Giancarlo D'Orazio for insightful discussions on this work, as well as Ben Inbar and Yeong Lee for their help with IV data collection. This work was performed in part at the Cornell NanoScale Facility, an NNCI member supported by NSF Grant NNCI-2025233. This work also made use of the Cornell Center for Materials Research Shared Facilities which are supported through the NSF MRSEC program (DMR-1719875). The data that support the findings of this study are available from the corresponding author upon request.

References

- [1] Lozano, P. C., Wardle, B. L., and Moloney, P., "Nanoengineered thrusters for the next giant leap in space exploration," *MRS Bulletin*, Vol. 40, 2015, pp. 842–849. <https://doi.org/10.1557/mrs.2015.226>.
- [2] Perez-Martinez, C. S., "Engineered Ionic Liquid Ion Sources for Ion Beam Applications," *Ph.D. Thesis, Massachusetts Institute of Technology*, 2016.
- [3] Fenn, J. B., Mann, M., Meng, C. K., and Wong, S. F., "Electrospray ionization-principles and practice," *Mass Spectrometry Reviews*, Vol. 9, 1990, pp. 37–70.
- [4] Vasiljevich, I., Tajmar, M., Grienauer, W., Plesescu, F., Buldrini, N., Amo, J. G. D., Carnicero-Dominguez, B., and Betto, M., "Development of an Indium mN-FEEP Thruster," *44th AIAA/ASME/SAE/ASEE Joint Propulsion Conference & Exhibit*, 2008.
- [5] Perez-Martinez, C. S., and Lozano, P., "Ion field-evaporation from ionic liquids infusing carbon xerogel microtips," *Applied Physics Letters*, Vol. 107, 2015. <https://doi.org/10.1063/1.4927481>.
- [6] MacArthur, J. V., "Material and Fabrication Developments in the Ion-Electrospray Propulsion System," *M.S. Thesis, Massachusetts Institute of Technology*, 2020.
- [7] Fischer, J., and Wegener, M., "Three-dimensional optical laser lithography beyond the diffraction limit," *Laser and Photonics Reviews*, Vol. 7, 2013, pp. 22–44. <https://doi.org/10.1002/lpor.201100046>.
- [8] Nanoscribe-GmbH, "Highest Resolution 3D Printing Spectrum of Applications New Trends in Microfabrication," 2018. URL <https://www.ncl.ac.uk/media/wwwnclacuk/nanolab/files/events/nanoscribe-highest-resolution-micro-3d-printer-details.pdf>.

- [9] Krpoun, R., Smith, K. L., Stark, J. P. W., and Shea, H. R., "Tailoring the hydraulic impedance of out-of-plane micromachined Electrospray sources with Integrated Electrodes," *AIP Publishing*, 2009. URL <https://aip.scitation.org/doi/10.1063/1.3117191>.
- [10] Callister, W. D., and Rethwisch, D. G., *Materials Science and Engineering*, 9th ed., Wiley, 2013.
- [11] Carrier, W. D., "Goodbye, Hazen; Hello, Kozeny-Carman," *Journal of Geotechnical and Geoenvironmental Engineering*, Vol. 129, No. 11, 2003, pp. 1054–1056. [https://doi.org/10.1061/\(ASCE\)1090-0241\(2003\)129:11\(1054\)](https://doi.org/10.1061/(ASCE)1090-0241(2003)129:11(1054)).
- [12] Kornev, K. G., and Neimark, A. V., "Spontaneous Penetration of Liquids into Capillaries and Porous Membranes Revisited," *Journal of Colloid and Interface Science*, Vol. 235, No. 1, 2001, pp. 101–113. <https://doi.org/https://doi.org/10.1006/jcis.2000.7347>.